1D Nanostructured Na$_7$V$_4$(P$_2$O$_7$)$_4$(PO$_4$) as High-Potential and Superior-Performance Cathode Material for Sodium-Ion Batteries

Chao Deng*,† and Sen Zhang*,‡

†Key Laboratory for Photonic and Electronic Bandgap Materials, Ministry of Education; College of Chemistry and Chemical Engineering, Harbin Normal University, Harbin, 150025, Heilongjiang China

‡College of Material Science and Chemical Engineering, Harbin Engineering University, Harbin 150001, Heilongjiang China

S *Supporting Information*

ABSTRACT: Tailoring materials into nanostructure offers unprecedented opportunities in the utilization of their functional properties. High-purity Na$_7$V$_4$(P$_2$O$_7$)$_4$(PO$_4$) with 1D nanostructure is prepared as a cathode material for rechargeable Na-ion batteries. An efficient synthetic approach is developed by carefully controlling the crystal growth in the molten sodium phosphate. Based on the XRD, XPS, TG, and morphological characterization, a molten-salt assisted mechanism for nanoarchitecture formation is revealed. The prepared Na$_7$V$_4$(P$_2$O$_7$)$_4$(PO$_4$) nanorod has rectangle sides and preferential [001] growth orientation. GITT evaluation indicates that the sodium de/intercalation of Na$_7$V$_4$(P$_2$O$_7$)$_4$(PO$_4$) nanorod involves V^{3+}/V^{4+} redox reaction and Na$_5$V$^{3.5+}$$_4$(P$_2O_7$)$_4$(PO$_4$) as intermediate phase, which results in two pairs of potential plateaus at the equilibrium potentials of 3.8713 V (V^{3+}/V$^{3.5+}$) and 3.8879 V (V$^{3.5+}$/V^{4+}), respectively. The unique nanoarchitecture of the phase-pure Na$_7$V$_4$(P$_2$O$_7$)$_4$(PO$_4$) facilitates its reversible sodium de/intercalation, which is beneficial to the high-rate capability and the cycling stability. The Na$_7$V$_4$(P$_2$O$_7$)$_4$(PO$_4$) cathode delivers 80% of the capacity (obtained at C/20) at the 10 C rate and 95% of the initial capacity after 200 cycles. Therefore, it is feasible to design and fabricate an advanced rechargeable sodium-ion battery by employment of 1D nanostructured Na$_7$V$_4$(P$_2$O$_7$)$_4$(PO$_4$) as the cathode material.

KEYWORDS: *1D nanostructure, mixed-polyanion material, Na$_7$V$_4$(P$_2$O$_7$)$_4$(PO$_4$), intermediate phase, sodium ion battery*

1. INTRODUCTION

High-performance materials are critical for the development of new alternative energy-storage systems. Lithium ion battery which has the highest energy density is a mature technology for energy storage, but its application is limited by disadvantages such as high cost and scarce resource of lithium.[1] Therefore, the employment of other guest ion as an alternative to lithium-ion is favorable to further development of the intercalation chemistry. The abundant resource and low cost of sodium make sodium-ion battery a promising alternative to lithium-ion battery.[2,3] However, the higher redox potential of Na/Na$^+$ lowers the cell voltage of sodium ion battery, at the same time the larger ionic radius of Na$^+$ makes it more difficult to find a suitable host for sodium ion de/intercalation.

Since 1980s, many materials have been studied as the intercalation hosts for Na ions. Layered oxides such as Na$_x$CoO$_2$,[4,5] Na$_x$FeO$_2$,[6] Na$_x$CrO$_2$,[7] and NaNi$_{1/3}$Mn$_{1/3}$Co$_{1/3}$O$_2$[8] are considered as promising cathode hosts for sodium intercalation. However, their unsatisfactory stability resulting from the structural collapse during sodium de/intercalation prohibits their practical application. In comparison with the layered oxide, the sodium containing polyanion and mix-polyanion compounds have more stable host frameworks, which result in their longer cycle life and better safety.[9–19] Recently, various phosphorus-based polyanion mateials such as
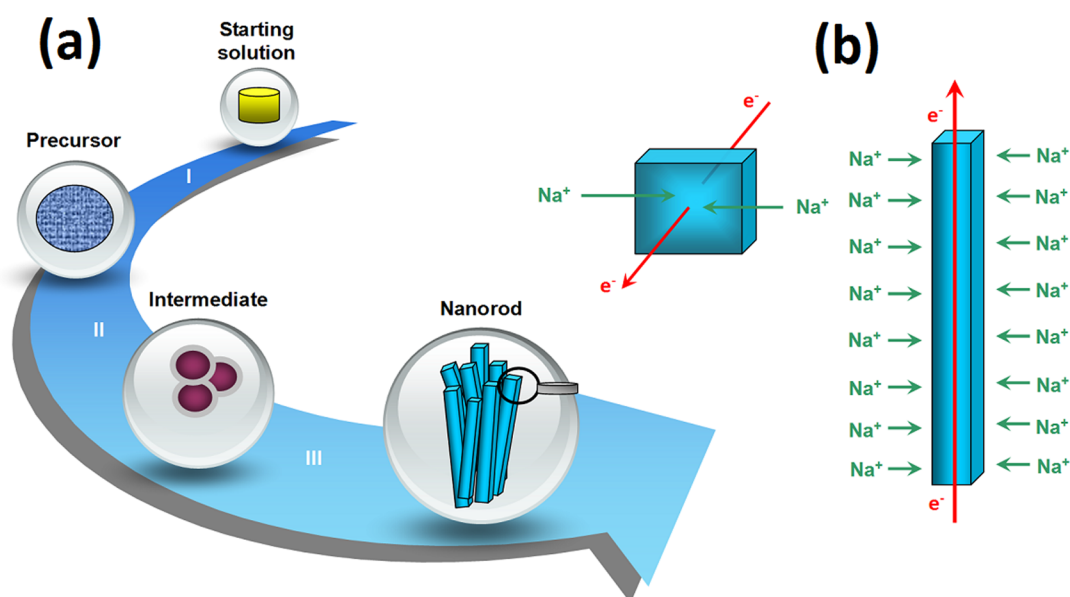
NaVOPO$_4$,[9] Na$_{4-\alpha}$M$_{2+\alpha/2}$(P$_2$O$_7$)$_2$ (M = Fe, Mn, Mn$_{0.5}$Fe$_{0.5}$),[10–12] Na$_4$Fe$_3$(PO$_4$)$_2$(P$_2$O$_7$),[13,14] and Na$_3$V$_2$(PO$_4$)$_3$[15–17] were reported to have good electrochemical performance. However, their sluggish sodium-intercalation kinetic and low operating voltage inhibits their practical application in sodium ion batteries. In the family of the mixed-polyanion compounds, Na$_7$V$_4$(P$_2$O$_7$)$_4$(PO$_4$) is a new member.[18] Its 3D framework structure provides well-defined ion diffusion channels for Na intercalation. Moreover, the high operating potential and the reversible phase transition during sodium de/intercalation process make it a promising cathode candidate for sodium ion batteries. However, conventional solid-state method results in the impurity containing Na$_7$V$_4$(P$_2$O$_7$)$_4$(PO$_4$) with poor morphological characteristics; thus, a feasible synthetic method is needed to prepare phase-pure Na$_7$V$_4$(P$_2$O$_7$)$_4$(PO$_4$) with well-defined particle morphology.

The "rocking chair" chemistry in sodium ion batteries involves both electron transfer and ionic diffusion. Nano-engineering is an effective strategy to facilitate the electron transfer and the ionic diffusion simultaneously.[20–26] Among the
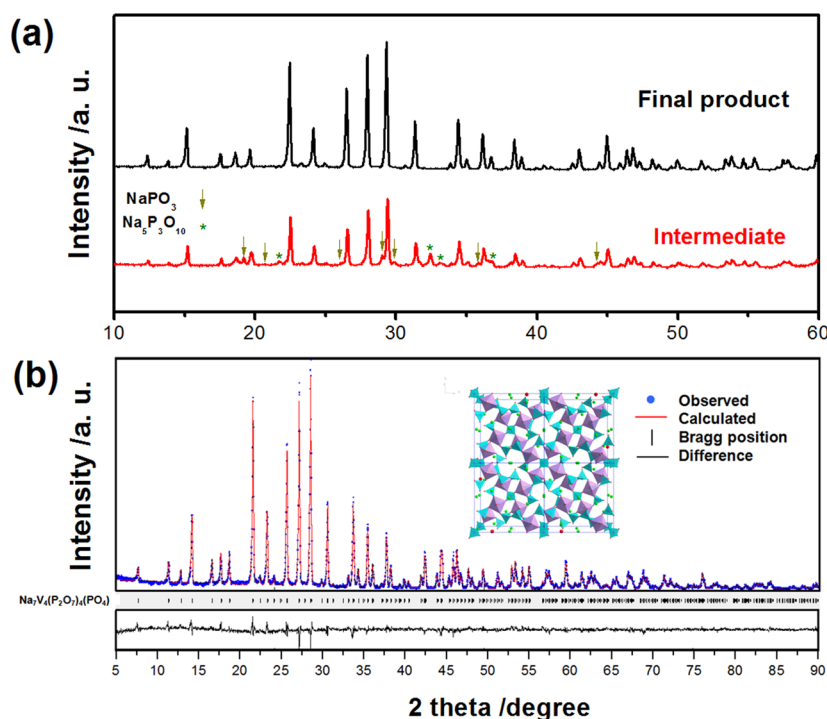
Figure 1. Schematic diagram illustrating (a) the synthetic process of the 1D nanostructured $Na_7V_4(P_2O_7)_4(PO_4)$ and (b) the pathways of charge transfer and ionic diffusion for a single nanorod with rectangle sides: (I) the sol−gel process, (II) the calcination process, (III) the purification process.
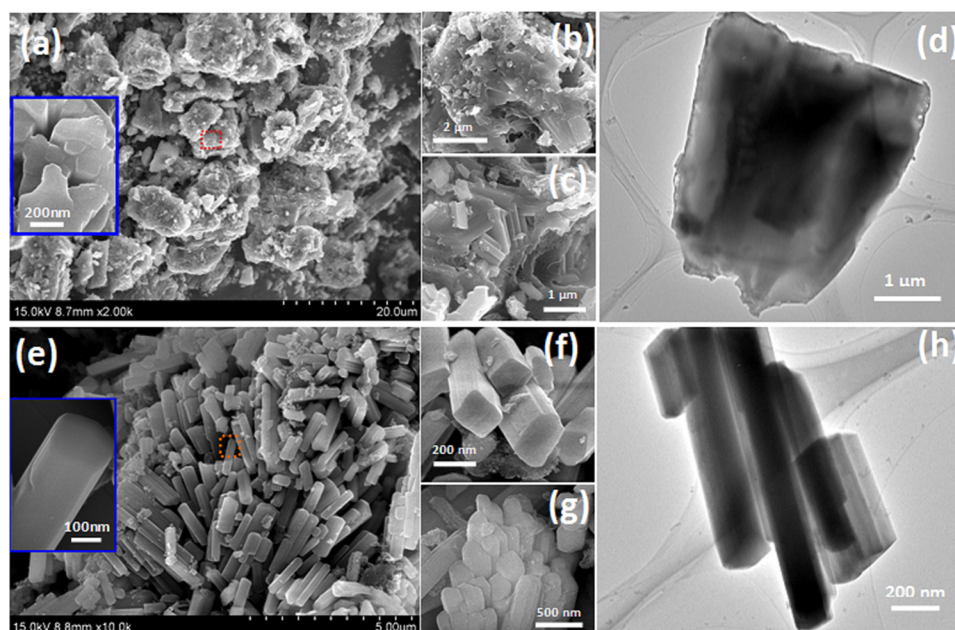

Figure 2. (a) XRD patterns of the multiphase intermediate product and the final product; (b) Retiveld refinement of the final product. The crystal structure of $Na_7V_4(P_2O_7)_4(PO_4)$ is illustrated as an inset of part b.

wide range of nanostructures, the 1D nanostructures such as nanowire,[23] nanorod,[24] and nanotube[25,26] have unique architectural characteristics, which exhibit significant advantages in energy-storage applications. The short solid-state pathway for ionic diffusion and the large surface area for charge transfer can effectively improve the electrochemical performance of the 1D nanoarchitectured intercalation host for sodium ion batteries.

Inspired by the advantages of the 1D nanostructure, for the first time, we design an efficient method to prepare the $Na_7V_4(P_2O_7)_4(PO_4)$ nanorods with rectangular sides. As illustrated in Figure 1a, the first step is a sol−gel process, and it results in a blue dry gel as the precursor. The second step is a high-temperature calcination process with programmed temperature ramps, and an intermediate multiphase product is obtained. The final step is a purification process, which results in the final product of phase-pure $Na_7V_4(P_2O_7)_4(PO_4)$ comprising of nanorods with rectangular sides. The pathways of electrons and sodium-ions within the prepared $Na_7V_4(P_2O_7)_4(PO_4)$ nanorod are illustrated in Figure 1b.

Figure 3. (a−c, e−g) SEM and (d, h) TEM images of the multiphase (a∼d) intermediate product and (e∼h) the final product. The enlarged images corresponding to red square in parts a and d are displayed as insets.

Sodium ions are expected to diffuse across the rectangluar sides of the nanorod, and electrons are expected to transfer along the nanorod. The short solid-state pathway for sodium-ion diffusion as well as the large surface area for electron transfer enables rapid sodium-ion de/intercalation, which is beneficial to its electrochemical performance.

2. EXPERIMENTAL SECTION

2.1. Synthesis. Stoichiometric amount of $NaHCO_3$, $NH_4H_2PO_4$, and NH_4VO_3 with the molar ratio of 1:1:0.308 and desired amount of citric acid were used as starting materials. All the reagents were dissolved in distilled water; the resulting solution was kept at 80 °C under magnetic stirring to evaporate water until it turned into a wet gel. The wet gel was dried at 100 °C overnight to obtain the dry gel which was grounded and subjected to programmed heat treatment in an argon atmosphere. The furnace temperature was increased from 20 to 850 °C at 10 °C min^{-1}, kept at 850 °C for 12 h, cooled to 500 °C at the rate of 5 °C min^{-1} and quenched to 20 °C. The resulting intermediate product was soaked in hot water with argon bubbling. After filtering, washing, and drying, the final product, that is, $Na_7V_4(P_2O_7)_4(PO_4)$, was obtained.

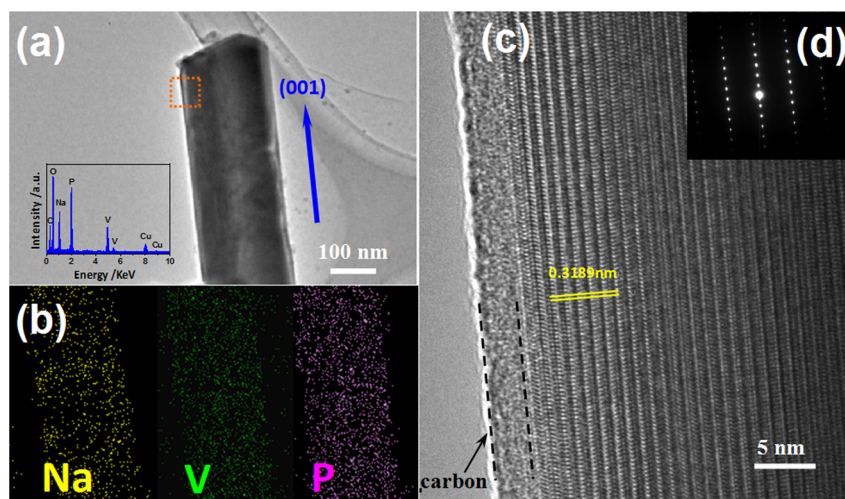**2.2. Materials Characterization.** Powder X-ray diffraction (XRD, Bruker D8/Germany) using Cu Kα radiation was employed to identify the crystalline phase of the material. The experiment was performed by using step mode with a fixed time of 3 s and a step size of 0.02°. The XRD pattern was refined by using the Rietveld method.[27] The morphology was observed with a scanning electron microscope (SEM, HITACHI S-4700) and a transmission electron microscope (TEM, JEOS-2010 PHILIPS), and the chemical composition was determined by an energy dispersive X-ray detector (EDX). X-ray photoelectron spectroscopy (XPS, Thermo ESCALAB 250) was employed to measure the chemical or electronic state of each element in the surface. Thermogravimetric analysis (TG/DSC, NETZSCH STA 449C) was carried out in flowing argon. The precursor was heated from 30 to 1070 °C at a rate of 5 °C min^{-1}. The carbon content in the $Na_7V_4(P_2O_7)_4(PO_4)$/C composite is about 1.2 wt %, which was determined by an elemental analyzer (EA, Elementar Vario EL).

2.3. Electrochemical Measurements. Coin cells were assembled to carry out the electrochemical measurements. The composite electrode was made from a mixture of the prepared sample, acetylene black, and polyvinylidene fluoride in a weight ratio of 70:20:10. A disk
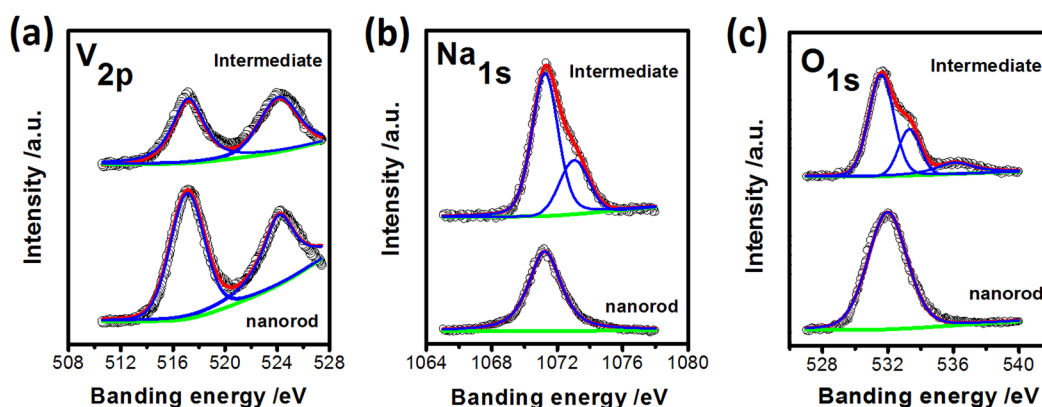
of sodium foil was used as counter electrode and 1 mol·L^{-1} $NaClO_4$ dissolved in propylene carbonate (PC) was used as electrolyte. For the galvanostatic intermittent titration technique (GITT), a constant current of 0.02 C was applied for 10 min, and then, it was interrupted to achieve the open circuit condition for 40 min. This process was repeated until the electrode potential reached the cutoff voltage. Galvanostatic charge−discharge tests were performed in the potential range of 2.5−4.1 V vs Na/Na$^+$ at ambient temperature on a Land battery testing system (Wuhan, China). All the specific capacities are calculated on the basis of $Na_7V_4(P_2O_7)_4(PO_4)$ only.

3. RESULTS AND DISCUSSION

The XRD patterns of the intermediate multiphase product (step II) and the final product (step III) are shown in Figure 2a. Two impurity phases (i.e., $NaPO_3$ and $Na_4P_2O_7$) are observed in the intermediate multiphase product. They are marked with arrows and asterisks, respectively. Both impurities are water-soluble Na−P−O salts. The possible existence of some amorphous Na−P−O phase cannot be excluded, which is perhaps another factor lowering the intensity of the XRD peaks. The impurities in the intermediate multiphase product is eliminated by hot water washing; thus, the final product is free from impurities. The XRD pattern of the phase-pure final product is refined to extract the structural details. As shown in Figure 2b, the final product has a tetragonal structure with a space group of $P\bar{4}2_1c$. The lattice parameters obtained by the Rietveld refinement are $a = 14.2281(3)$ Å and $c = 6.3733(2)$ Å (R_p = 10.05%, R_{wp} = 13.31%). The crystal structure of $Na_7V_4(P_2O_7)_4(PO_4)$ is illustrated as an inset of Figure 2b. The 3D framework of $[V_4(P_2O_7)_4(PO_4)]_\infty$ is constructed through each $[PO_4]$ tetrahedron sharing corners with four adjacent $[VO_6]$ octahedra and each $[P_2O_7]$ group sharing corners with two adjacent $[VO_6]$ octahedral.[18] Three different interstitial sites (i.e., Na1, Na2, and Na3) are occupied by sodium ions. Sodium ions can diffuse along the well-defined channels in the 3D framework, which enables the reversible sodium de/intercalation and thus is favorable to realize good electrochemical performance.

Figure 4. (b) Element mapping, (c) HRTEM image, and (d) SEAD pattern of the single nanorod illustrated in part a. The EDS spectrum and the schematic diagram of the nanorod are shown as insets of part a.
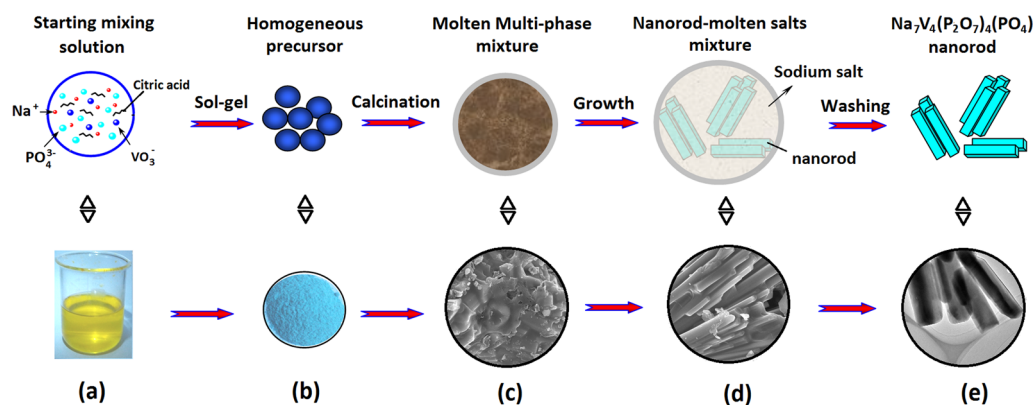

Figure 5. XPS spectra of V 2p (a), Na 1s (b), and O 1s (c) of the multiphase intermediate product and the final product.

The SEM and TEM images of the intermediate multiphase product (step II) and final product (step III) are shown in Figure 3. Irregular particles ranging from 3 to 20 μm were observed in the SEM image of the intermediate multiphase product (Figure 3a). Initial enlargement of the large particle reveals its porous coarse surface (Figure 3b), further enlargement discovers some nanorods with smooth surface, which are embedded in the large particle (Figure 3c). The TEM image of the intermediate multiphase product also indicates their complex morphological characteristics (Figure 3d). The final product is composed of nanorods with rectangular sides (Figure 3e~h). The length of the nanorods can reach 2 μm, while the side length of the rectangular cross-section resides in the range 150−200 nm.
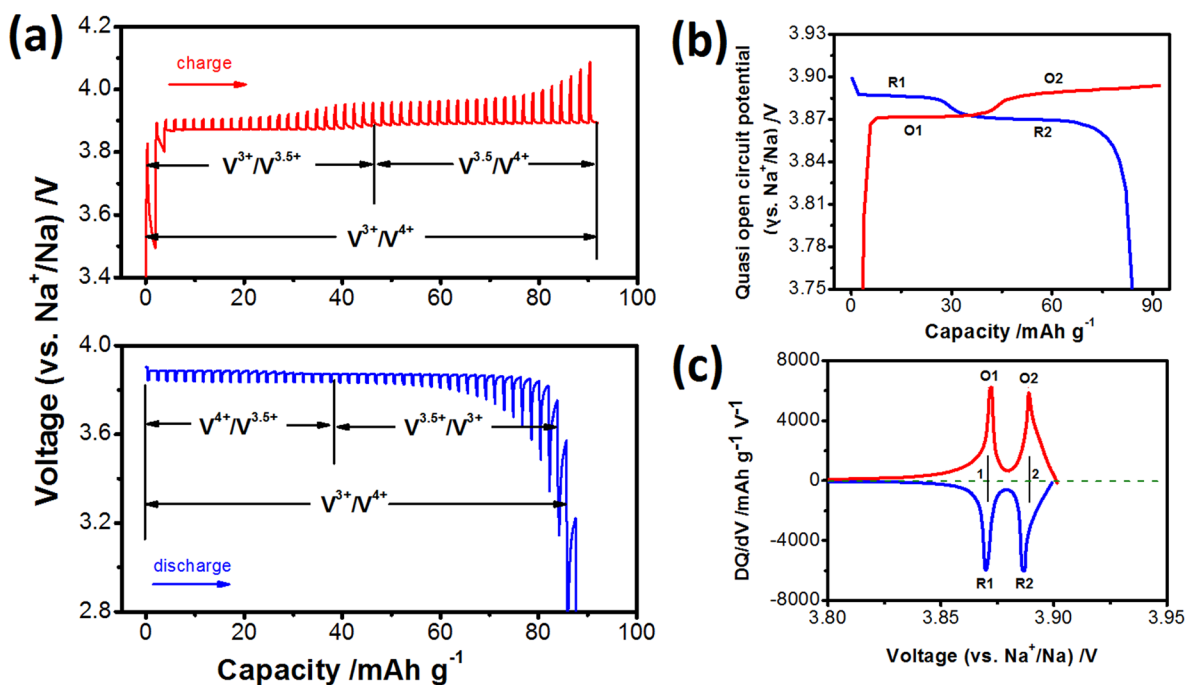
High resolution TEM (HRTEM), microscopic elemental analysis and selected area electron diffraction (SAED) were further employed to extract more microscopic information from the 1D nanostructure. Na, V, and P is uniformly distributed over the $Na_7V_4(P_2O_7)_4(PO_4)$ nanorod, and their atomic ratio is equal to 7:4:9 which is consistent with the theoretical value (Figure 4a,b). As shown in the HRTEM image (Figure 4c), the interplanar distance of 0.32 nm corresponds to the (002) plane of the tetragonal structure, and moreover, an amorphous carbon layer of ~2 nm attached to the surface is also detected. On the basis of the above observation, this material has a nanorod shape and the intersection of the rod is

almost square, indicating that the four longitudinal rectangular planes are symmetrically identical. The square intersection plane should be perpendicular to the [001] direction if the rod has a 4-fold symmetry. Therefore, the preferential growth direction of the nanorod is deduced to be [001], which is perpendicular to the [002] plane. The SEAD pattern also confirms the single crystal nature of the nanorod, which is in accordance with the HRTEM observation.

The XPS spectra of the intermediate multiphase product (step II) and the final product (step III) were collected to provide more information on the physicochemical change in the synthetic process. Both V 2p spectra have two peaks which are centered at 517.1 and 523.4 eV, respectively (Figure 5a); this indicates that the oxidation states of V in both products are +3.[28] However, the peaks in the spectrum of the final product are stronger than those in the spectrum of the intermediate multiphase product, which indicates that the vanadium concentration on the surface is increased by the purification process (step III). The Na−P−O salts are removed and the surfaces of the $Na_7V_4(P_2O_7)_4(PO_4)$ nanorods are exposed, which also results in some change in the Na 1s and O 1s spectra (Figure 5b,c). Both the Na 1s and O 1s spectra of the final product show a single-peak character, which indicates that both Na and O in the $Na_7V_4(P_2O_7)_4(PO_4)$ nanorods have a single oxidation state, respectively. However, both the Na 1s and O 1s spectra of the intermediate multiphase product have a strong

9114

dx.doi.org/10.1021/am501072j | ACS Appl. Mater. Interfaces 2014, 6, 9111−9117

Figure 6. Mechanism of the synthetic method: (a) the homogeneous solution, (b) the dry gel precursor, (c) the molten mixture, (d) the multiphase intermediate product, (e) the final product.

Figure 7. GITT evaluation of the $Na_7V_4(P_2O_7)_4(PO_4)$ nanorod: (a) the GITT charge and discharge curves, (b) the QOCP charge and discharge curves, (c) the differential capacity vs voltage (dQ/dV) curves calculated from part b.
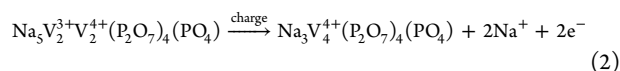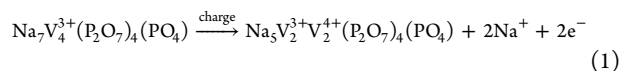
asymmetric peak, which can be separated into two well-defined peaks. The additional peaks in the Na 1s and O 1s spectra can be attributed to the Na and O in the Na−P−O salts, respectively. The results of XPS are consistent with those of XRD and SEM, that is to say, the Na−P−O salts are totally removed by the purification process (step III). The Na−P−O salts partially cover the surface of the $Na_7V_4(P_2O_7)_4(PO_4)$ nanorods and bind them together to form large secondary particles.

The approach employed in this study is identified as an efficient route to prepare phase-pure $Na_7V_4(P_2O_7)_4(PO_4)$ with 1D nanostructure; thus, it is necessary to uncover the underlying mechanism, which guarantees the effectiveness of this approach. The possible mechanism is depicted in Figure 6. At the initial stage, the homogeneous colloids are prepared by a sol−gel process with all the starting materials (Figure 6a,b). Then, the premature calcination results in a molten mixture (Figure 6c). Supported by the thermal analysis, the molten mixture is formed after the evaporation of water ($T < 200\ °C$)

and the decomposition of the organic species ($200\ °C < T < 600\ °C$) (Supporting Information Figure S1). After that, nucleation and growth of the nanostructured particles take place in the molten phase under surpersaturation. The growth of the $Na_7V_4(P_2O_7)_4(PO_4)$ nanorod is boosted when the molten mixture is kept at 850 °C. The complete calcination process results in an intermediate multiphase product that consists of the $Na_7V_4(P_2O_7)_4(PO_4)$ nanorods and the Na−P−O salts covered on its surface (Figure 6d). Finally, the Na−P−O salts are removed by hot water and the phase-pure $Na_7V_4(P_2O_7)_4(PO_4)$ nanorods are obtained (Figure 6e). The element stoichiometry and the temperature ramp must be carefully controlled to optimize the composition of the molten mixture and the growth of the $Na_7V_4(P_2O_7)_4(PO_4)$ nanorods, which plays an important role in determining the shape and purity of the final product.
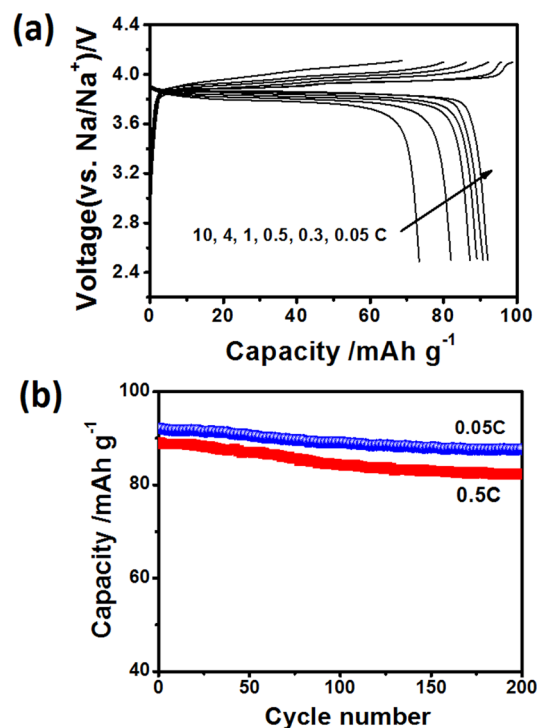
The electrochemical performance of the $Na_7V_4(P_2O_7)_4(PO_4)$ nanorods as cathode material for sodium ion batteries was evaluated using coin-type cells. First of all, GITT measurement

was carried out to clarify the nature of sodium de/intercalation (Figure 7a). The quasi-open-circuit potential (QOCP) upon charge and discharge is picked out from the GITT curve and plotted against the capacity (Figure 7b). Both the charge and discharge curves have two potential plateaus and each plateau corresponds to a phase transition process. In the charge curve, the capacities of the two potential plateaus are nearly equal, which indicates the existence of $Na_5V_4(P_2O_7)_4(PO_4)$ as an intermediate phase between the two terminal phases (i.e., $Na_7V_4(P_2O_7)_4(PO_4)$ and $Na_3V_4(P_2O_7)_4(PO_4)$). Therefore, the average oxidation state of V in $Na_5V_4(P_2O_7)_4(PO_4)$ is +3.5. These results are consistent with those reported by Lim et al., who attribute the formation of the intermediate phase to the ordering of Na^+, V^{3+}, and V^{4+}.[18] The reactions in the process of sodium extraction can be described by the following two equations:

$$Na_7V_4^{3+}(P_2O_7)_4(PO_4) \xrightarrow{charge} Na_5V_2^{3+}V_2^{4+}(P_2O_7)_4(PO_4) + 2Na^+ + 2e^- \tag{1}$$

$$Na_5V_2^{3+}V_2^{4+}(P_2O_7)_4(PO_4) \xrightarrow{charge} Na_3V_4^{4+}(P_2O_7)_4(PO_4) + 2Na^+ + 2e^- \tag{2}$$

The QOCP vs capacity curve is differentiated to get the differential capacity (dQ/dV) vs voltage curve (Figure 7c). The oxidation/reduction peaks in Figure 7c correspond to the charge/discharge plateaus in Figure 7b. As shown in Figure 7c, each oxidation peak is paired with a reduction peak. The O1/R1 pair can be attributed to the phase transition between $Na_7V_4(P_2O_7)_4(PO_4)$ and $Na_5V_4(P_2O_7)_4(PO_4)$ whose equilibrium potential is 3.8713 V, while the O2/R2 pair can be attributed the phase transition between $Na_5V_4(P_2O_7)_4(PO_4)$ and $Na_3V_4(P_2O_7)_4(PO_4)$ whose equilibrium potential is 3.8879 V. The high operating potential of $Na_7V_4(P_2O_7)_4(PO_4)$ makes it a promising cathode material for sodium ion batteries.

The rate capability and cycling performance are summarized in Figure 8. Various current densities (i.e., 0.05 C, 0.3 C, 0.5 C, 1 C, 4 C, and 10 C) are employed to evaluate the rate capability. The charge/discharge curve at each current density is shown in Figure 8a. When the current density is 0.05 C, two plateaus can be observed in the charge curve. When the current density is higher, the plateaus become vaguer, indicating larger polarization. A discharge capacity as high as 92.1 mAh·g^{-1} is obtained at the current density of 0.05 C, which is very close to the theoretical capacity of $Na_7V_4(P_2O_7)_4(PO_4)$ (92.8 mAh·g^{-1}). Although the discharge capacity declines with an increase in current density, nearly 80 percent of the theoretical capacity (i.e., 73 mAh·g^{-1}) is realized at the current density of 10 C. The superb rate capability of the $Na_7V_4(P_2O_7)_4(PO_4)$ nanorods can be attributed to its high purity and well-defined morphology. Short sodium-ion diffusion pathway as well as large electron transfer area enables rapid sodium-ion extraction and insertion. The long-term cycling performances at the current densities of 0.05 and 0.5 C are shown in Figure 8b; the capacity retentions after 200 cycles are 95.2% and 92.6%, respectively. After the cycling test, the $Na_7V_4(P_2O_7)_4(PO_4)$ nanorods were recovered and subjected to XRD measurement. The XRD pattern of the cycled material is similar to that of the original material (Supporting Information Figure S2), which indicates that the structure of the $Na_7V_4(P_2O_7)_4(PO_4)$ nanorods undergoes little change upon repeated sodium de/intercalation. Therefore, the high cycling stability results from the excellent structural stability. The good electrochemical performance of the 1D

Figure 8. Electrochemical performance of the $Na_7V_4(P_2O_7)_4(PO_4)$ nanorods: (a) the charge/discharge curves at different current density in the voltage range 2.5−4.1 V; (b) the long-term cycling performance at 0.05 C and 0.5 C.

nanostructured $Na_7V_4(P_2O_7)_4(PO_4)$ can be attributed to its favorable structural and morphological characteristics.

4. CONCLUSIONS

The phase-pure $Na_7V_4(P_2O_7)_4(PO_4)$ with 1D nanostructure is introduced as a high-performance cathode materials for sodium ion batteries. By carefully controlling the element stoichiometry and the temperature ramp, we design an efficient approach to prepare the high-quality $Na_7V_4(P_2O_7)_4(PO_4)$ nanorods, which is favorable to rapid sodium intercalation. Based on the XRD, XPS, TG, SEM, and TEM results, a molten salt assisted synthetic mechanism for the nanoarchitecture formation is revealed. The resultant material acquires high purity and 1D nanostructure with rectangle sides. The existence of $Na_5V_4(P_2O_7)_4(PO_4)$ as an intermediate phase is indicated by GITT evaluation because two oxidation/reduction plateaus are observed in the charge/discharge curve. It is demonstrated by the differential capacity analysis that the equilibrium transition potentials of $Na_7V_4(P_2O_7)_4(PO_4)/Na_5V_4(P_2O_7)_4(PO_4)$ and $Na_5V_4(P_2O_7)_4(PO_4)/Na_3V_4(P_2O_7)_4(PO_4)$ are 3.8713 and 3.8879 V, respectively. The favorable structural and morphological characteristics of the $Na_7V_4(P_2O_7)_4(PO_4)$ nanorods enable it to have good electrochemical performance such as large reversible capacity, superb rate capability, and high cycling stability. The high operating potential together with the excellent electrochemical performance make the $Na_7V_4(P_2O_7)_4(PO_4)$ nanorod a promising cathode material for advanced sodium ion batteries.

■ ASSOCIATED CONTENT

S Supporting Information

TG analysis of the precursor, XRD patterns of the cycled $Na_7V_4(P_2O_7)_4(PO_4)$. This material is available free of charge via the Internet at http://pubs.acs.org/.

■ AUTHOR INFORMATION

Corresponding Authors
*Email: chaodeng2008@yahoo.cn; chaodenghsd@sina.com. Tel: 86-451-88060570.
*Email: senzhang@hrbeu.edu.cn. Tel: 86-451-82589186.
Notes
The authors declare no competing financial interest.

■ REFERENCES

(1) Ong, S.; Chevrier, V.; Hautier, G.; Jain, A.; Moore, C.; Kim, S.; Ma, X.; Ceder, G. Voltage, Stability, and Diffusion Barrier Differences between Sodium-Ion and Lithium-Ion Intercalation Materials. *Energy Environ. Sci.* **2011**, *4*, 3680−3688.

(2) Buchholz, D.; Moretti, A.; Kloepsch, R.; Nowak, S.; Siozios, V.; Winter, M.; Passerini, S. Toward Na-Ion Batteries-Synthesis and Characterization of a Novel High Capacity Na Ion Intercalation Material. *Chem. Mater.* **2013**, *25*, 142−148.

(3) Palomares, V.; Cabanas, M. C.; Martinez, E. C.; Han, M. H.; Rojo, T. Update on Na-Based Battery Materials. A Growing Research Path. *Energy Environ. Sci.* **2013**, *6*, 2312−2337.

(4) Braconnier, J.; Delmas, C.; Fouassier, C.; Hagenmuller, P. Comportement Electrochimique Des Phases Na_xCoO_2. *Mater. Res. Bull.* **1980**, *15*, 1797−1804.

(5) Berthelot, R.; Carlier, D.; Delmas, C. Electrochemical Investigation of the P2−Na_xCoO_2 Phase Diagram. *Nat. Mater.* **2011**, *10*, 74−80.

(6) Blesa, M.; Moran, E.; Leon, C.; Santamaria, J.; Tornero, J.; Menendez, N. α-$NaFeO_2$: Ionic Conductivity and Sodium Extraction. *Solid State Ion.* **1999**, *126*, 81−87.

(7) Braconnier, J.; Delmas, C.; Hagenmuller, P. Etude Par Desintercalation Electrochimique Des Dystemes Na_xCrO_2 and Na_xNiO_2. *Mater. Res. Bull.* **1982**, *17*, 993−1000.

(8) Sathiya, M.; Hemalatha, K.; Ramesha, K.; Tarascon, J.; Prakash, A. Synthesis, Structure, and Electrochemical Properties of the Layered Sodium Insertion Cathode Material: $NaNi_{1/3}Mn_{1/3}Co_{1/3}O_2$. *Chem. Mater.* **2012**, *24*, 1846−1853.

(9) Song, J.; Xu, M. W.; Wang, L.; Goodenough, J. B. Exploration of $NaVOPO_4$ as a Cathode for a Na-Ion Battery. *Chem. Commun.* **2013**, *49*, 5280−5282.

(10) Kim, H.; Shakoor, R. A.; Park, C.; Lim, S. Y.; Kim, J. S.; Jo, Y. N.; Cho, W.; Miyasaka, M.; Jung, Y.; Choi, J. W. $Na_2FeP_2O_7$ as a Promising Iron-Based Pyrophosphate Cathode for Sodium Rechargeable Batteries: A Combined Experimental and Theoretical Study. *Adv. Funct. Mater.* **2013**, *23*, 1147−1155.

(11) Park, C.; Kim, H.; Shakoor, R.; Yang, E.; Lim, S.; Kahraman, R.; Jung, Y.; Choi, J. Anomalous Managanese Activation of a Pyrophosphate Cathode in Sodium Ion Batteries: A Combined Experimental and Theoretical Study. *J. Am. Chem. Soc.* **2013**, *135*, 2787−2792.

(12) Ha, K. H.; Woo, S. H.; Mok, D. G.; Choi, N. S.; Park, Y.; Oh, S. M.; Kim, Y.; Kim, J.; Lee, J.; Nazar, L. F.; Lee, K. T. $Na_{4−\alpha}M_{2+\alpha/2}(P_2O_7)_2$ ($2/3 \leq \alpha \leq 7/8$, M = Fe, $Fe_{0.5}Mn_{0.5}$, Mn): A Promising Sodium Ion Cathode for Na Ion Batteries. *Adv. Energy Mater.* **2013**, *3*, 770−776.

(13) Kim, H.; Park, I.; Seo, D. H.; Lee, S.; Kim, S. W.; Kwon, W. J.; Park, Y. U.; Kim, C. S.; Jeon, S.; Kang, K. New Iron-Based Mixed-Polyanion Cathodes for Lithium and Sodium Rechargeable Batteries: Combined First Principles Calculations and Experimental Study. *J. Am. Chem. Soc.* **2012**, *134*, 10369−10372.

(14) Kim, H.; Park, I.; Lee, S.; Kim, H.; Park, K. Y.; Park, Y. U.; Kim, H.; Kim, J.; Lim, H. D.; Yoon, W. S.; Kang, K. Understanding the Electrochemical Mechanism of the New Iron Based Mixed Phosphate $Na_4Fe_3(PO_4)_2(P_2O_7)$ in a Na Rechargeable Battery. *Chem. Mater.* **2013**, *25*, 3614−3622.

(15) Jung, Y. H.; Lim, C. H.; Kim, D. K. Graphene-Supported $Na_3V_2(PO_4)_3$ as a High Rate Cathode Material for Sodium-Ion Batteries. *J. Mater. Chem. A* **2013**, *1*, 11350−11354.

(16) Saravanan, K.; Mason, C. W.; Rudola, A.; Wong, K. H.; Balaya, P. The First Report on Excellent Cycling Stability and Superior Rate Capability of $Na_3V_2(PO_4)_3$ for Sodium Ion Batteries. *Adv. Energy Mater.* **2013**, *3*, 440−450.

(17) Lim, S.; Kim, H.; Shakoor, R.; Jung, Y.; Choi, J. Electrochemical and Thermal Properties of Nasicon Structured $Na_3V_2(PO_4)_3$ as a Sodium Rechargeable Battery Cathode: A Combined Experimental and Theoretical Study. *J. Electrochem. Soc.* **2012**, *159*, A1393−A1397.

(18) Lim, S. Y.; Kim, H.; Chung, J.; Lee, J. H.; Kim, B. G.; Choi, J. J.; Chung, K. Y.; Cho, W.; Kim, S. J.; Goddard, W. A.; Jung, Y. S.; Choi, J. W. Role of Intermediate Phase for Stable Cycling of $Na_7V_4(P_2O_7)_4(PO_4)$ in Sodium Ion Battery. *Proc. Natl. Acad. Sci. U.S.A.* **2014**, *111*, 599−604.

(19) Barpanda, P.; Nishimura, S.; Yamada, A. High Voltage Pyrophosphate Cathodes. *Adv. Energy Mater.* **2012**, *2*, 841−859.

(20) Wang, D. P.; Belharouak, I.; Zhou, G. W.; Amine, K. Nanoarchitecture Multi-structural Cathode Materials for High Capacity Lithium Batteries. *Adv. Funct. Mater.* **2013**, *23*, 1070−1075.

(21) Tepavcevic, S.; Xiong, H.; Stamenkovic, V. R.; Zuo, X. B.; Balasubramanian, M.; Prakapenka, V. B.; Johnson, C. S.; Rajh, T. Nanostructured Bilayered Vanadium Oxide Electrodes for Rechargeable Sodium-Ion Batteries. *ACS Nano* **2012**, *6*, 530−538.

(22) Croce, F.; Appetecchi, G. B.; Persi, L.; Scrosati, B. Nanocomposite Polymer Electrolytes for Lithium Batteries. *Nature* **1998**, *394*, 456−458.

(23) Chen, Z.; Augustyn, V.; Jia, X. L.; Xiao, Q. F.; Dunn, B.; Lu, Y. F. High-Performance Sodium-ion Pseudocapacitors Based on Hierarchically Porous Nanowire Composites. *ACS Nano* **2012**, *6*, 4319−4327.

(24) Deng, C.; Zhang, S.; Dong, Z.; Shang, Y. 1D Nanostructured Sodium Vanadium Oxide as a Novel Anode Material for Aqueous Sodium Ion Batteries. *Nano Energy* **2014**, *3*, 14−19.

(25) Yin, J.; Qi, L.; Wang, H. Y. Sodium Titanate Nanotubes as Negative Electrode Materials for Sodium-ion Capacitors. *ACS Appl. Mater. Interfaces* **2012**, *4*, 2762−2768.

(26) Cao, Z. Y.; Wei, B. Q. V_2O_5/Single-Walled Carbon Nanotube Hybrid Mesoporous Films as Cathodes with High-Rate capacities for Rechargeable Lithium Ion Batteries. *Nano Energy* **2013**, *2*, 481−490.

(27) Lutterotti, L.; Scardi, P. Simultaneous Structure and Size Strain Refinement by the Rietveld Method. *J. Appl. Crystallogr.* **1990**, *23*, 246−252.

(28) Zhang, S.; Wu, Q.; Deng, C.; Liu, F. L.; Zhang, M.; Meng, F. L.; Gao, H. Synthesis and Characterization of Ti−Mn and Ti−Fe Codoped $Li_3V_2(PO_4)_3$ as Cathode Material for Lithium Ion Batteries. *J. Power Sources* **2012**, *218*, 56−64.